Cement and Concrete Research 100 (2017) 398–412

Contents lists available at ScienceDirect

Cement and Concrete Research

journal homepage: www.elsevier.com/locate/cemconres

Recycling of hydrated cement pastes by synthesis of α'_H-C_2S

Ricardo Serpell[a,*], Franco Zunino[b,1]

[a] Department of Construction Engineering and Management, School of Engineering, Pontificia Universidad Católica de Chile, Santiago, Chile
[b] Department of Civil Engineering, Faculty of Engineering, Universidad del Desarrollo, Av. La Plaza 680, Las Condes, Santiago, Chile

ARTICLE INFO

Keywords:
Thermal treatment
Ca_2SiO_4
X-ray diffraction
Crystal size
Waste management

ABSTRACT

Hardened cement paste in concrete wastes can be a valuable precursor material for the production of recycled cements. In the reported study, X-ray diffraction data of cementitious materials obtained by thermal processing of hardened pastes were quantitatively analyzed using Rietveld refinement to explain the effect of process parameters on their hydration reactivity and on the strength gain of pastes made with them. The parameters studied were annealing temperature, residence time, and cooling rate. Across the annealing temperature range explored C_2S polymorphs were found to comprise the larger fraction of the resulting materials. However, their relative concentrations varied. Results indicate alpha'$_H$-C_2S formed at low temperature is highly reactive and remains stable on cooling due to its smaller crystallite size, whereas at higher temperatures most of it converts to the less reactive beta-C_2S on cooling. Accordingly, materials obtained at lower temperatures exhibited higher heats of hydration and much higher strength gain rates.

1. Introduction

Even though concrete is not a particularly contaminating material, it has a large impact on the environment due to the large quantity being produced every year. Recycling has the potential to reduce all of the main aspects of concrete environmental impact: the consumption of natural resources and energy, the emissions of carbon dioxide and the generation of solid wastes. Production of recycled aggregates has already been shown to effectively reduce the pressure of concrete manufacturing on natural aggregate sources and the pressure of construction and demolition wastes on available landfills. However, the largest part of energy consumption and CO_2 emissions are associated with the cement production [1]. Considering Portland cement is the higher costing component of concrete, both in economic and environmental terms, significant benefits could be achieved by recycling the hydrated cement fraction of the concrete wastes. Hydrated cement paste (HCP) remains partly adhered to crushed concrete aggregates and concentrates in the finer sized fraction due to the higher surface to volume ratio of the smaller aggregate particles. Since residual HCP in the recycled aggregates degrades the performance of new concrete, several crushing steps are usually implemented to improve the separation. The byproduct is crushed concrete fines with a high concentration of HCP.

In practice, different recycled materials can be developed based on different degrees of processing of the fines, with higher degrees requiring higher energy input. At the lower energy end of the range, the fines can be used as a low value filler material. At the opposite end, the fines can be used as a raw material for the production of new Portland cement Clinker [2–4]. Unless original concrete has been exposed to severe chemical attack or environmental weathering, the oxide composition of the HCP should match that of the cement it was made with. Major constituents of HCP are cement hydration products: calcium silicate hydrates (C-S-H), Portlandite and hydrated calcium sulfates, plus any unreacted cement remaining. Analogously as in the case of clinker raw materials, when powdered HCP is heated, Belite (C_2S) is the first calcium silicate formed in solid state reactions occurring below 1200 °C. However, whereas in the materials resulting from heating of clinker raw meals to 800 °C beta-C_2S is the most abundant polymorph of C_2S present [5], a significant fraction of alpha'-C_2S was identified in materials obtained by heating of HCP to the same temperature [6]. Due to the presence of this more reactive polymorph of C_2S, materials obtained by heating and annealing HCP to around 800 °C display significant cementitious behavior [7,8]. This behavior opens up the possibility of recycling the cement fraction of concrete wastes producing reactivated cementitious materials by thermal processing of HCP at temperatures much lower than those required to produce clinker.

In a previous study it was shown that the relationship between annealing temperature and cementitious behavior of the reactivated materials correlated with the relative concentration of alpha'-C_2S in them [6]. Qualitative analysis of X-ray diffraction (XRD) profiles of the reactivated materials showed alpha'-C_2S related peaks increased in

* Corresponding author.
E-mail addresses: rserpell@ing.puc.cl (R. Serpell), franco.zunino@epfl.ch (F. Zunino).
[1] Current address: Laboratory of Construction Materials, EPFL STI IMX LMC Station 12, CH-1015 Lausanne, Switzerland.

http://dx.doi.org/10.1016/j.cemconres.2017.08.001
Received 18 January 2017; Received in revised form 31 July 2017; Accepted 3 August 2017

intensity with increasing annealing temperature in the range 600 to 800 °C. Above 800 °C the peaks were seen to change in position and intensity towards the pattern of beta-C_2S. Concurrently, mortars made with reactivated materials annealed at 800 °C achieved higher 28-day strengths. Regression models for 7-day strength of the mortars predicted somewhat lower optimal annealing temperatures, but this was considered as due to larger variance of the 7-day strength results. The study did not distinguish between the two main forms of alpha′-C_2S observed in pure C_2S: alpha′$_H$-C_2S stable above 1160 °C and alpha′$_L$-C_2S, stable above 630–680 °C. Although the XRD pattern best fitting the observed profile was from a phosphate stabilized form of alpha′-C_2S, the precise cause for the stabilization at room temperature of this high temperature polymorph could not be determined from the results of the qualitative analysis.

The study reported in this manuscript focused on quantitatively characterizing the effect of additional parameters of the thermal process on the relative abundance and crystal structure characteristics of the phases in the resulting materials. Considering phase formation and polymorph transformations are thermodynamically controlled processes, in addition to annealing temperature, residence time and cooling rate were considered, as they are expected to affect the phase composition of the reactivated materials. By simultaneously characterizing the effect of the said process parameters on the cementitious behavior of the materials, the study aimed at stablishing stronger relationships between phase composition and material performance. Phase composition and crystal structure characteristics were studied by quantitative analysis of powder X-ray diffraction (QXRD) by whole pattern fitting using the Rietveld method [9]. Cementitious behavior was studied by isothermal conduction calorimetry of hydration reactions up to 7 days, and by compressive strength testing of neat pastes made with the resulting materials up to 90 days of hydration. A new method for the mixing of reactivated material pastes was developed that avoids the negative effects of rapid free Lime hydration and allows mixing at lower effective water to cement ratios.

2. Experimental design, materials and methods

2.1. Experimental design

The experimental region of interest was defined to partly encompass the combination of factor levels that had been explored in previous studies. The ranges of experimental levels for the annealing temperature, residence time and cooling rate, were thus centered at 800 °C, 90 min and −10 °C/min, respectively. Response surface methodology was selected to explore the experimental region around this central point. The combinations of factor levels in the experiment were defined using a rotatable central composite design for 3 factors which enables efficient use of least squares regression to produce second order response surface models [10] (Fig. 1). The core of the design is a full factorial experiment in two levels that allows estimation of the linear effects of factors and factor interactions. This core is augmented with two axial cases for each factor (at factor levels exceeding the range covered in the factorial part) which allow estimation of the second order effects of the factors, and multiple replications of a central case (at the center level of all factors) which allow estimation of the experimental variance. In response surface models derived from rotatable designs, the variance of the predicted response is a function of the distance from the center of the design only. This is a desirable feature when the behavior of the response in the experimental region is not known in advance. In central composite designs each factor is applied in five coded levels: $-\alpha$, −1, 0, 1, α, where α is the coded level of the factor at the axial cases. Choosing $\alpha = (n_f)^{1/4}$, where n_f is the number of factorial cases in the design, a rotatable design is obtained. Therefore, in the selected design $\alpha = 1.682$. The coded and experimental levels of the factors, annealing or maximum temperature (factor X1: m_temp), residence time (X2: r_time) and cooling rate (X3: c_rate) for all cases in

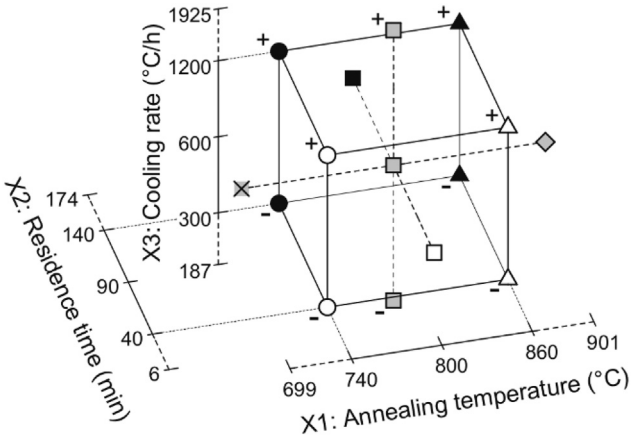

Fig. 1. Central composite experimental design defined for the study, showing the range and combination of factor levels explored across the experimental region. The symbols displayed at every design point provide a key to identify cases or groups of cases having specific factor levels in the result plots shown in the following figures.

the experimental design are shown in Table 1. Cooling rate levels where based on a logarithmic scale, with the central level set to match the rate applied during heating (10 °C/min). The experiment was divided in two blocks: Block A, comprising the factorial cases and three central case replicates, were executed first followed by Block B, comprising the axial case and two central case replicates. Execution of cases within each block was randomized.

2.2. Precursor materials and thermal treatments

For the purposes of this study, precursor materials for the thermal reactivation process were obtained from a single batch of cement paste produced using ordinary (type I) Portland cement and distilled water. Elemental composition of the Portland cement was determined by X-ray fluorescence, using a Bruker S8 Tiger wavelength dispersive spectrometer. Cement samples were cast in Lithium-Borate glass beads using a Claisse M4 gas fluxer. The paste was mixed at a 0.5 water to cement ratio (by weight) and molded into slab-like forms approximately 600 by 400 by 40 mm in size. The hardened cement paste obtained was unmolded after 24 h and placed under lime-saturated water to cure. After 28 days of curing, the hydrated cement paste (HCP) slabs were crushed into irregular pieces of 40 mm maximum dimension. Hydration was stopped by drying the material at 105 °C until constant weight was achieved. The pieces were then reduced in size using a jaw crusher and then powdered in a ball mill in batches of 2.5 kg each. The number of mill revolutions required to achieve a material with 90% of particles under 100 μm in size (equivalent volume sphere diameter) was determined by sampling the first batch at fixed intervals. Samples were analyzed in a Malvern Mastersizer 2000 laser diffraction particle size analyzer, dispersed in water and using sonication to improve dispersion. The number of revolutions thus determined was applied to all subsequent batches. Powdered precursor material was kept in a sealed container until the time of thermal processing.

Thermal treatments according to the experimental design were carried out in a Nabertherm HT-16/40 programmable electric furnace equipped with motorized exhaust flap and drought fan that enables controlled forced cooling. Every process involved heating, annealing and cooling of 640 g of precursor material, distributed in 8 crucibles of 150 ml capacity (80 g of precursor material in each), arranged in two lines of four roughly centered in the oven chamber (both horizontally and vertically). A type K (chromel-alumel) thermocouple embedded in the material of one of the centermost crucibles was used to monitor the temperature evolution of the charge in each of the thermal processes applied (Fig. 2). The maximum temperature and cooling rate set values in the thermal process programs were adjusted according to results

Table 1
Coded and experimental levels of factors in the experimental design.

Case ID	Exec. order	Factor levels						
		Coded			Experimental			
		X1: m_temp	X2: r_time	X3: c_rate	X1: m_temp	X2: r_time	X3: c_rate	
					(°C)	(min)	ln (−°C/h)	(−°C/h)
A_01	7	−1	−1	−1	740	40	5.70	300
A_02	2	1	−1	−1	860	40	5.70	300
A_03	1	−1	1	−1	740	140	5.70	300
A_04	8	1	1	−1	860	140	5.70	300
A_05	10	−1	−1	1	740	40	7.09	1200
A_06	11	1	−1	1	860	40	7.09	1200
A_07	4	−1	1	1	740	140	7.09	1200
A_08	5	1	1	1	860	140	7.09	1200
A_09	3	0	0	0	800	90	6.40	600
A_10	6	0	0	0	800	90	6.40	600
A_11	9	0	0	0	800	90	6.40	600
B_12	19	−1.682	0	0	699	90	6.40	600
B_13	16	1.682	0	0	901	90	6.40	600
B_14	13	0	−1.682	0	800	6	6.40	600
B_15	18	0	1.682	0	800	174	6.40	600
B_16	15	0	0	−1.682	800	90	5.23	187
B_17	12	0	0	1.682	800	90	7.56	1925
B_18	14	0	0	0	800	90	6.40	600
B_19	17	0	0	0	800	90	6.40	600

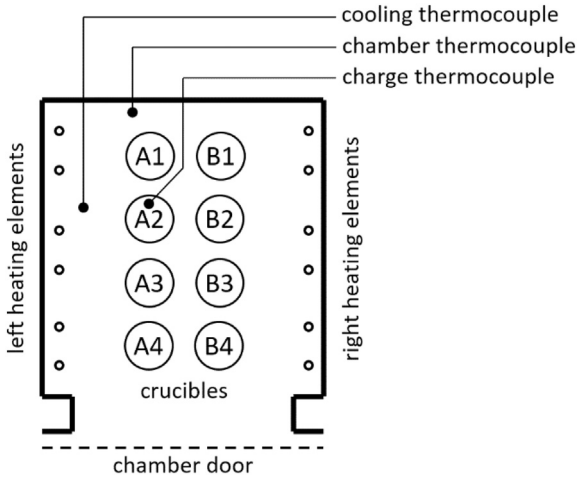

Fig. 2. Schematic diagram of charged oven, showing approximate location of thermocouples used to control and monitor the thermal process.

from preliminary tests using the described setup. Overall, maximum temperatures were reduced by 20 °C compared to the target values in the design, and cooling rates were set according to the empirical approximation: $k_C = k_0\ (1 + k_0 / 3000)$, where, k_C is the adjusted (programmed) cooling rate and k_0 is the target cooling rate. The largest target cooling rate (−1925 °C/h) was approximated by removing the material from the oven at the end of the annealing period and air quenching it over a stainless steel tray. Fig. 3 shows the recorded temperature of the materials during cooling for the cases comprising the factorial part of the experimental design compared to their target cooling rates. In order to prevent spontaneous hydration involving air moisture, reactivated materials were stored in sealed containers while still at temperatures above 100 °C. After cooling resulting materials were accurately weighed to determine the mass loss experienced by the material during the process. The loss on ignition (LOI) was calculated as the mass loss over the ignited (post-process) mass.

2.3. Analysis of reactivated materials

Precursor materials and reactivated materials obtained in every case of the experimental design were analyzed by powder X-ray diffraction (XRD) in Bragg-Brentano geometry. Two data sets were obtained independently using different instruments. Profiles in the first data set were obtained in a Bruker D8 diffractometer equipped with a Co Kα source working at 40 kV/30 mA, in the range 10° to 75° 2theta (0.62 to 4.27 $Å^{-1}$), using a step size of 0.02° 2theta with an exposure time of 0.5 s per step. Fluorite (CaF_2, Sigma Aldrich 449717) was intermixed by hand at around 5% by weight (accurately measured) to each sample in order to estimate the fraction of material explained by the analysis (i.e. crystalline phases identified and quantified) by the internal standard method [11,12]. This method was selected over the external standard method due to lack of direct access to the diffraction instrument (third party lab services were used for this data set). The powdered materials were back-loaded in the sample holders to minimize preferred orientation, using 3 kN of force. The second set of XRD data for all materials was obtained using a Bruker D2 Phaser diffractometer equipped with a Cu Kα source working at 30 kV/10 mA, and a solid state LinxEye detector, in the range 10° to 90° 2theta (0.71 to 5.76 $Å^{-1}$), using a step size of 0.01° 2theta with an equivalent exposure time of 0.5 s per step. This second data set was intended to provide additional data, and over a wider 2theta angle range, to improve the initial refinement of the structure models of the phases present. Accordingly, no standard was intermixed in the materials and, in addition to the precursor and reactivated materials, the set included the Portland cement, the Fluorite standard and a Corundum standard target used for instrument parameter refinement. An averaged profile was compiled from the second-set XRD profiles of the 5 central cases in the experiment to help with phase identification and initial structure model refinement for the phases present in the reactivated materials. The profiles were aligned before averaging them by minimizing the sum of squared count differences over the whole 2theta range.

Identification of phases was carried out on the second-set XRD profiles of the Portland cement, the HCP, the averaged central case, and the axial cases (i.e. those at the extreme levels of the factors). Software

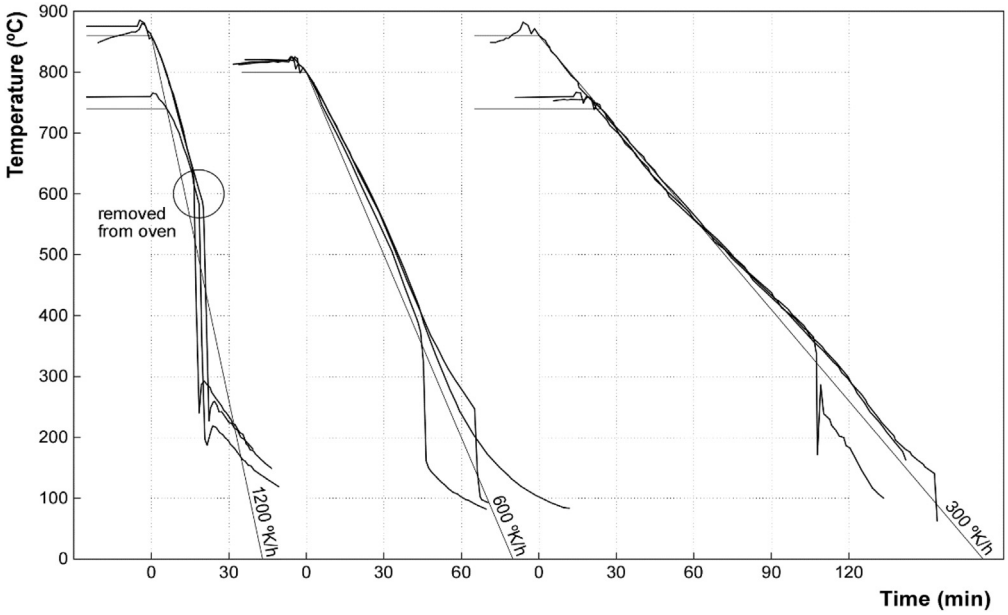

Fig. 3. Recorded temperature of materials during cooling compared to the target cooling rates defined in the experimental design.

Table 2
Phases identified in precursor and reactivated materials.

	Formula	Crystal system	Reference	Year
Alite (C_3S)	Ca_3SiO_5	Monoclinic, M_3	De la Torre et al. [17]	2002
Belite (β-C_2S)	Ca_2SiO_4	Monoclinic, β	Mumme et al. [18]	1995
(α'_H-C_2S)	Ca_2SiO_4	Orthorhombic, α'_H	Mumme et al. [18]	1995
(γ-C_2S)	Ca_2SiO_4	Orthorhombic, γ	Mumme et al. [18]	1995
Ferrite (C_4AF)	Ca_2AlFeO_5	Orthorhombic	Berliner et al. [19]	1997
Aluminate (C_3A)	$Ca_{7.95}Na_{1.74}Al_6O_{17.82}$	Orthorhombic	Berliner et al. [19]	1997
Lime	CaO	Cubic	Wyckoff, R.W.G. [20]	1963
Portlandite	$Ca(OH)_2$	Trigonal	Desgranges et al. [21]	1993
Calcite	$CaCO_3$	Trigonal	Effenberger et al. [22]	1981
Gypsum	$CaSO_4.2H_2O$	Monoclinic	Cole & Lancucki [23]	1974
Bassanite	$CaSO_4.0.5H_2O$	Monoclinic	Ballirano et al. [24]	2001
Anhydrite	$CaSO_4$	Orthorhombic	Morikawa et al. [25]	1975
Mayenite	$Ca_{12}Al_{14}O_{33}$	Cubic	Palacios et al. [26]	2007
Ternesite	$Ca_5(SiO_4)2SO_4$	Orthorhombic	Irran et al. [27]	1997
Periclase	MgO	Cubic	Wyckoff, R.W.G. [20]	1963

Match! by Crystal Impact GbR was used, together with a locally assembled database comprising patterns generated from crystal structure models for cement phases available from the Materials and Structural Systems Division of the National Institute of Standards and Technology [13] and crystal structure models for inorganic compounds from the Crystallography Open Database [14]. Quantitative analysis of the XRD results was performed by Rietveld refinement. This whole profile fitting method involves the use of least squares to minimize the residual function, i.e. the weighted sum of squared differences between the observed experimental profile and a theoretical profile calculated from crystal structure models of the phases present in the sample and a model of the experimental setup. The minimization is an iterative process involving varying degrees of user input. Selected parameters of the models are progressively refined until the agreement between experimental and calculated profiles satisfies a predefined criterion. The selection of parameters to be refined depends on the unknowns that need to be determined. A detailed description of the method, including the common sources of error when used for the quantification of phases in anhydrous cement can be found in [15]. Rietveld refinements were carried out using software MAUD [16], pursuing a target goodness of fit (*sigma*) below 2.0. Structure models used are shown in Table 2.

The quantitative analysis was divided in two parts. First, relevant crystal structure models were refined using the second set of XRD data. The profile of the Corundum target was used to refine parameters related to the instrument setup. Resulting refined values for the relative intensities of the incident X-rays and for the peak shape function of the instrument were used in the analysis of all profiles from the same data set. In addition to quantitative phase analysis, the profile of the Portland cement was used for the refinement of parameters of structure models of the anhydrous cement phases. Refinement included: lattice parameters for all phases present above 1% by weight, and crystallite size and micro-strain of the major constituent phases of cement: tri-calcium silicate (C_3S), di-calcium silicate (C_2S), tetra-calcium alumino-ferrite (C_4AF) and tri-calcium aluminate (C_3A). Atomic coordinates of C_3S were also refined as this significantly improved the fit and provided a better structure model to later quantify this phase in the reactivated materials. For a cement paste mixed at 0.5 water to cement ratio, after only 28 days of hydration, a fraction of the major constituent phases of the cement is expected to remain anhydrous. Quantitative analysis was used to estimate their relative abundance in the HCP. Being formed at temperatures exceeding those of the thermal process under study, most anhydrous phases present in the HCP should remain largely unchanged by the process, the exception being C_2S polymorphs which are expected to form and transform at this temperature range. The initial structure refinement included lattice parameters and crystallite sizes for all phases exceeding 10% by weight. In addition, atom positions were refined for alpha'$_H$-C_2S and beta-C_2S. The set of pre-refined structure models obtained was assembled as a control

Table 3
Analysis of Portland cement used to produce the precursor materials.

Oxide analysis		
Oxide	XRF	
	In cement	In clinker
	wt%	wt%[a]
CaO	63.61	61.55
SiO_2	21.34	21.15
Al_2O_3	3.78	3.68
Fe_2O_3	3.02	3.02
SO_3	2.84	0.33
MgO	1.82	1.82
Na_2O	0.53	0.53
K_2O	0.45	0.45
TiO_2	0.33	0.33
P_2O_5	0.19	0.19
MnO	0.06	0.06
SrO	0.15	0.15
ZnO	0.01	0.01
Cr_2O_3	0.01	0.01
LOI	1.58	
Residue (est.)	0.30	
Total	100.00	93.26
Al_2O_3/Fe_2O_3		1.25
$SO_3/(Na_2O + K_2O)$	(Molar)	0.30
Ca/Si ratio		2.91

Phase composition				
Phase	QXRD			Modified Bogue
	1 data	2 data	Averg.	
	wt%	wt%	wt%	wt%
C_3S	67.47	71.98	69.72	66.61
C_2S	5.72	6.45	6.08	10.66
C_4AF	9.35	9.37	9.36	7.52
C_3A	7.59	7.93	7.76	6.88
Subtotal	90.12	95.73	92.93	91.67
Periclase	0.02	0.13	0.07	
Gypsum	0.27	0.47	0.37	
Bassanite	6.08	3.10	4.59	
Portlandite	2.47	0.56	1.52	
Calcite	1.04	< 0.01	0.52	
Total	100.00	100.00	100.00	
Expl. (%)	92.00	–		
Sigma	1.766	1.587		
Ca/Si ratio			3.01[b]	

[a] Estimated according to procedures found in [15].
[b] Reverse calculated using the modified Bogue method [14].

file for subsequent use in the analysis of the first set of XRD data.

In the second part, the control file previously obtained was used for the quantitative analysis of the first-set of XRD data. The parameters of the instrument contribution to peak shape were refined on the profiles of the central cases, by fixing the already refined crystallite size of the phases present. The refined instrument parameters were fixed for the rest of the analysis. Background contribution was modeled using a 4th order polynomial function. Quantitative analysis involved the following general steps:

1. Refinement of scale factors (all phases), background coefficient and 2theta offset. After convergence, phases below 0.5% by weight fraction were removed from the analysis.
2. Refinement of lattice parameters of C_2S polymorphs exceeding 10% by weight fraction.
3. Refinement of crystallite size of all phases present above around 5% by weight, except for original cement phases.
4. Refinement of scale factor, lattice parameters and crystallite size of additional phases identified in the profile which were not included in the control file.

These steps were cumulative, meaning parameters refined at every step are also refined in the subsequent steps. For most materials, refinement involved several iterations of the above step list.

2.4. Mixing procedure: pastes for calorimetry and strength tests

Reactivated materials are known to demand a large amount of water to achieve a workable consistency. In addition, the exothermal hydration of free calcium oxide present in them raises the initial temperature of the pastes, increasing their evaporation rates. Accordingly, in previous research high water to solids ratios have been used to achieve flowability requirements and to enable proper compaction of pastes or mortars made with reactivated materials. Unfortunately this also results in longer setting times and lower strengths. A two stage mixing protocol that lowers the water demand of the mixtures was developed in this study. The original purpose of the method was to compensate for water lost to evaporation during mixing due to heat released by the hydration of free calcium oxide. In order to have precise control of the water to solids ratio of the resulting paste, the water was added to the reactivated material in two batches, adjusting the final batch according to the weight loss due to evaporation. The final batch of water was added only after the mixture had cooled to room temperature. Several trials were carried out to determine if the proportion between batches had an effect on the characteristics of the resulting paste. Flowability was observed to increase when the initial batch was reduced compared to the final, apparently reaching a maximum when the initial batch was approximately 0.15 g of water per gram of reactivated material.

For every case in the experimental design a single batch of approximately 100 ml of mixture was produced to obtain paste for calorimetry and strength testing. Approximately 15 g of distilled water were gradually sprayed over 100 g of reactivated material on a plastic beaker, stirring continuously to ensure that all the dry material comes into contact with the humidity. The mixture remains a dry powder but the temperature in the beaker rapidly increases. After the mixture had cooled to room temperature it was weighed to determine the amount of water remaining. Additional water was then added to achieve the target water to solids ratio. Pastes were mixed for 60 s using a hand mixer at 18,000 rpm. A water to solids ratio of 0.7 by mass was selected for the central cases of the experimental design, equivalent to a volumetric water to solids ratio of 2.19 (considering the median density of the central cases). For the rest of the mixtures, the amount of reactivated material was adjusted according to the density of the reactivated material to keep the volumetric ratio constant, in order to maintain a fair comparison base for early-age performance between the mixtures [28]. Density of reactivated materials was measured by Nitrogen pycnometry using a Quantachrome Ultrapyc 1200e.

2.5. Isothermal calorimetry and strength tests

Isothermal calorimetry tests of the reactivated material pastes were performed using a TAM Air isothermal calorimeter configured at 23 °C. Glass ampoules were filled with approximately 10 g of sample (accurately measured) immediately after mixing (< 7 min after contact with final batch of water). Heat flow was measured continuously for 7 days. The amount of heat released normalized by the initial volume of water (J/ml w.) was used as an indicator of the initial development of mechanical properties, as this parameter has been shown to linearly correlate with compressive strength [29,30], even at different curing temperatures [31].

The rest of the paste was cast in nine 20 mm cubic molds. The cubic specimens were cured in the molds in an atmosphere of 100% relative humidity and 21 °C for 3 days and then unmolded and placed under lime-saturated water at 21 °C until testing time. Compressive strength tests were carried out on the saturated cubic specimens at a constant crosshead speed of 1.5 mm/min, at 7, 28 and 90 days of hydration. Polyamide-imide (PAI) plastic sheet pieces, 0.8 mm thick, were used as pads between press plates and specimen faces under load. Three specimens were tested at each age.

3. Results and discussion

Oxide analysis obtained from the XRF of the Portland cement used to produce the hydrated precursor material is shown in Table 3. Considering the fabrication process of the precursor material and the thermal processes involved in the reactivation, the relative abundances of major oxides in the HCP and in the reactivated materials is expected to largely resemble that of the original Portland cement. Abundancies of major constituent phases estimated from the results of the oxide analysis by the modified Bogue calculation [32] differ from the results of the quantitative analysis of the XRD data for this cement (also in Table 3). Overall, the calculation overestimates C_2S and underestimates C_4AF compared to the QXRD results, which indicates the substitutions estimated for both phases in the Bogue calculation are offset from their actual values. Overall, either analysis shows a cement with a relatively low concentration of C_2S compared with most Portland cements [5], probably well below 10% by weight. According to the QXRD analysis, calcium carbonate is present below 1% by weight and free calcium oxide is absent.

A rough estimate for the amount of unreacted cement in the hydrated precursor materials can be obtained comparing the average mass loss of the cases treated to higher temperatures, (18.1% of their ignited mass, as shown later), with the range of non-evaporable water contents expected for a fully hydrated type I Portland cement paste (21% to 23% of the mass ignited to 1000 °C [5]). Disregarding ignition temperature differences, an estimated 14% to 21% of the original cement mass remained unreacted in the precursor materials before the thermal processing. In fact, all major constituent phases of cement were identified in the XRD profile of the HCP. According to the QXRD analysis their relative concentrations in the HCP are: 35.4% C_3S, 23.5% C_2S, 30.5% C_4AF and 10.6% C_3A. Assuming from the previous estimation an unreacted fraction of 17.5% by weight of original cement, the unreacted fractions of each phase in the HCP would be 8.9%, 68.9%, 57.2% and 23.8% of the original C_3S, C_2S, C_4AF and C_3A masses, respectively. As expected by their relatively slower hydration kinetics, most of the original C_2S and C_4AF remain unreacted in the 28-day old paste. This large unreacted fraction, however, represented < 10% of the original mass due to the low concentration of either phase in the original cement. Despite the many assumptions of the previous estimates, they indicate that unreacted cement in the precursor material cannot explain the observed strength gain of pastes made with reactivated materials. In addition, they show that the total concentration of C_2S in the reactivated materials bears no relation to the concentration of unreacted C_2S in the precursor material and therefore new C_2S polymorphs are formed during the thermal process.

3.1. Thermal processing, calorimetry and strength test results and factor effects (regression)

As shown in Table 4, with the exception of case B_14, differences between average temperatures recorded in the materials during the annealing period and the design annealing temperatures in each case were generally below 15 °C (leaving case B_14 out, the standard deviation of recorded from design temperatures was 8.6 °C). The time-temperature record of B_14 shows the material did not reach the specified annealing temperature due to the short residence time specified for this case (6 min). In records from all experimental cases the charge temperature is seen to lag behind the oven chamber temperature. By the time the 6 min residence time had finished the material temperature in case B_14 had reached only 754 °C, instead of the 800 °C specified in the design. Considering that the recorded temperature closely corresponds to a coded level of − 1 for the annealing temperature factor, in the regression of the response models the coded levels considered for case B_14 were: − 1, − 1.682 and 0, for factors X1: m_temp, X2: r_time

Table 4
Results of thermal process, calorimetry and strength tests.

ID	Thermal process			Pastes mixed at ~0.7 w/s mass ratio				
	Annealing temp.		LOI (%)	Total heat released		Compressive strength		
	Design (°C)	Record (°C)		24 h (J/ml w.)	7 days (J/ml w.)	7 days (MPa)	28 days (MPa)	90 days (MPa)
A_01	740	750	16.33	111.3	265.8	20.7	28.2	31.5
A_02	860	844	18.32	28.8	112.9	1.6	23.7	30.5
A_03	740	754	17.39	119.0	261.0	23.8	29.9	32.0
A_04	860	867	18.04	17.6	71.4	1.0	10.8	21.3
A_05	740	749	16.72	111.2	259.1	21.3	26.2	31.6
A_06	860	848	17.68	29.8	106.0	2.5	15.5	22.1
A_07	740	755	17.67	121.7	256.3	24.2	31.2	29.9
A_08	860	869	18.21	16.6	71.9	0.8	9.0	19.1
A_09	800	813	17.80	42.8	169.4	11.1	24.9	26.8
A_10	800	806	17.63	61.8	173.6	10.0	22.6	25.9
A_11	800	805	17.90	69.0	188.3	12.2	23.8	26.7
B_12	699	717	16.33	108.4	259.8	21.2	27.5	31.6
B_13	901	898	17.68	12.1	66.4	0.8	9.2	18.7
B_14	800	754	16.07	105.1	254.2	20.9	29.0	32.6
B_15	800	813	17.63	50.2	154.0	9.6	29.6	29.9
B_16	800	808	16.87	66.7	191.3	13.8	27.0	30.2
B_17	800	805	17.43	67.7	181.0	11.1	23.3	24.8
B_18	800	807	16.64	65.1	182.1	12.0	25.5	26.8
B_19	800	812	17.63	69.9	201.8	15.0	24.0	28.8
Min.			16.07	12.1	66.4	0.8	9.0	18.7
Mean			17.37	67.1	180.3	12.3	23.2	27.4
Max.			18.32	121.7	265.8	24.2	31.2	32.6
Mean std. deviation between cube specimens (%)						4.00	5.16	8.68

Table 5
Loss on ignition (LOI), calorimetry and strength response model coeficcients (effects of thermal process parameters). Significant effects (coefficients with *p*-values ≤ 0.05) are marked in bold.

Factor	LOI		Heat 24-hour		Heat 7-day		Strength 7-day		Strength 28-day		Strength 90-day	
	Effect (%)	p-Value	Effect (J/ml w.)	p-Value	Effect (J/ml w.)	p-Value	Effect (MPa)	p-Value	Effect (MPa)	p-Value	Effect (MPa)	p-Value
X0: constant	**17.47**	**0.0000**	**61.1**	**0.0000**	**183.1**	**0.0000**	**12.0**	**0.0000**	**24.5**	**0.0000**	**27.2**	**0.0000**
First order												
X1: m_temp	**0.46**	**0.0007**	**− 39.2**	**0.0000**	**− 73.7**	**0.0000**	**− 8.8**	**0.0000**	**− 6.3**	**0.0000**	**− 3.9**	**0.0000**
X2: r_time	**0.25**	**0.0254**	− 3.2	0.4671	− 11.9	0.0672	− 0.2	0.8107	**− 1.1**	**0.0418**	**− 1.3**	**0.0122**
X3: c_rate	0.08	0.3522	0.3	0.9384	− 2.6	0.6454	− 0.2	0.8330	**− 1.2**	**0.0229**	**− 1.6**	**0.0028**
Interactions												
X1·X2	− 0.20	0.1018	− 4.6	0.3829	− 8.2	0.2509	− 0.8	0.5249	**− 3.5**	**0.0002**	**− 1.6**	**0.0085**
X1·X3	− 0.14	0.2468	− 0.3	0.9506	0.6	0.9316	0.0	0.9679	− 1.2	0.0771	− 1.1	0.0588
X2·X3	0.09	0.4662	0.1	0.9835	1.2	0.8693	− 0.2	0.8914	1.2	0.0703	0.5	0.3318
Second order												
X1·X1	− 0.09	0.3522	1.1	0.7956	− 6.8	0.2506	− 0.2	0.8215	**− 2.7**	**0.0003**	− 0.9	0.0524
X2·X2	0.01	1.0000	1.3	0.7697	− 1.8	0.7575	− 0.1	0.9444	**1.6**	**0.0084**	**1.3**	**0.0103**
X3·X3	− 0.04	0.6032	3.3	0.4348	1.2	0.8259	0.2	0.8107	− 0.2	0.6030	0.0	0.9749

and X3: c_rate, respectively. Similar, but smaller, correlations between residence time and recorded annealing temperature are observed for materials annealed at low temperature for long residence times (cases A_03 and A_07): exceeding design annealing temperatures by 14.5 °C on average, and for materials annealed at high temperature for short residence times (cases A_02 and A_06): below design annealing temperatures by 14.0 °C on average. These smaller correlations were not explicitly considered in the factor level matrix of the regressions. However, they are very important for the correct interpretation of results due to the large effect of annealing temperature on all material responses studied.

Second order regression of experimental results was used to characterize the effects of annealing temperature, residence time and cooling rate on the responses. The linear or second order effect of a factor or factor interaction corresponds to its regression coefficient. Analysis of variance was used to identify significant effects. In the following discussion, only the regression coefficients having p-values < 0.05 (5% significance level) are considered as significant effects of the thermal process parameters on the responses. Relatively large coefficients not reaching the significance criteria are also discussed for their potential effect on the responses. Annealing temperature (X1: m_temp) appears as the only factor having a significant effect on all observed responses. Accordingly, most of the graphs accompanying the following discussion plot material responses versus recorded annealing temperature. The symbol set shown in Fig. 1 is used in all of them in order to facilitate reading of other factor levels applied at each data point.

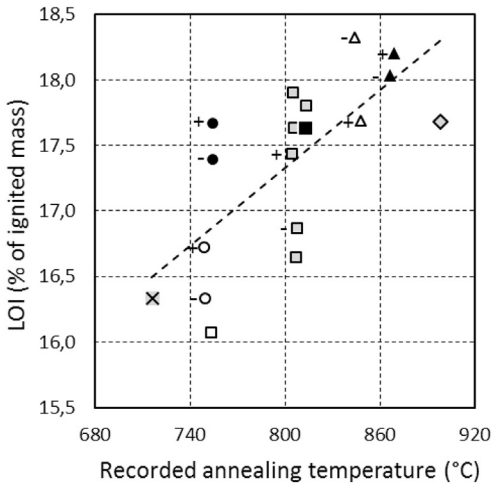

Fig. 4. Loss on ignition due to thermal processing versus annealing temperature.

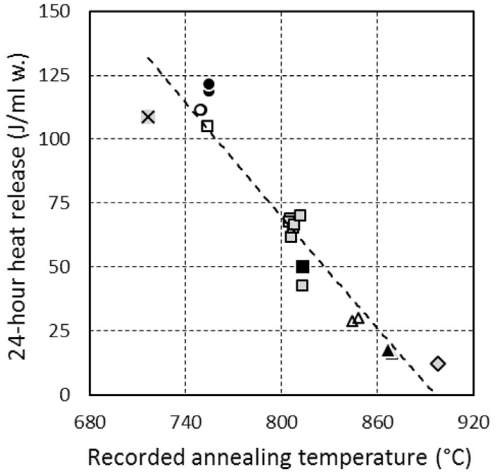

Fig. 5. Normalized heat released by reactivated material pastes over 24 h versus reactivated material annealing temperature.

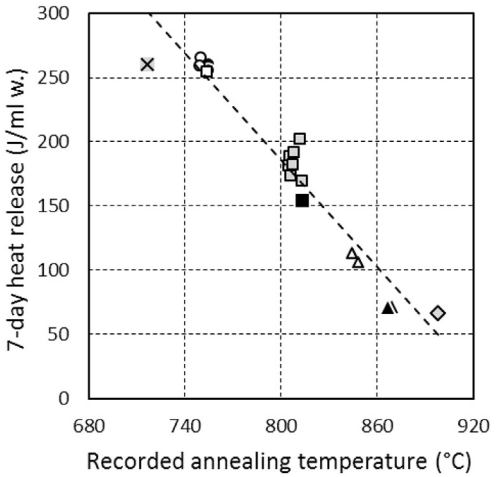

Fig. 6. Normalized heat released by reactivated material pastes over 7 days versus reactivated material annealing temperature.

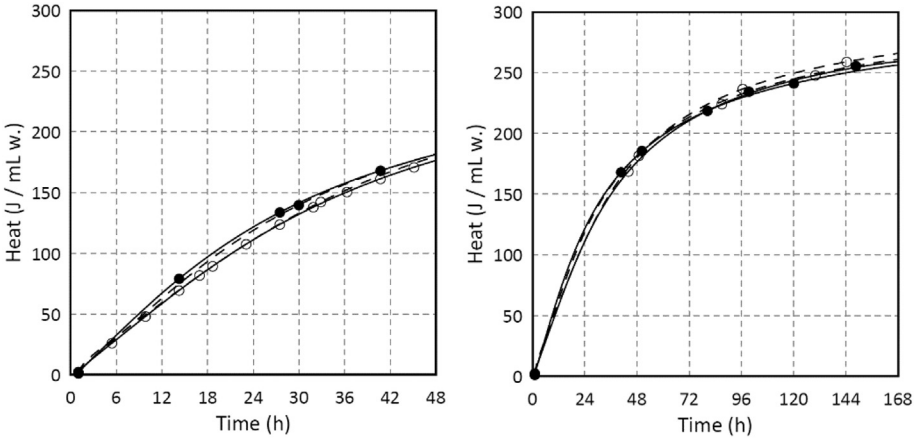

Fig. 7. Calorimetry results (total normalized heat released over time) for pastes produced with materials annealed at lower temperatures (~740 °C).

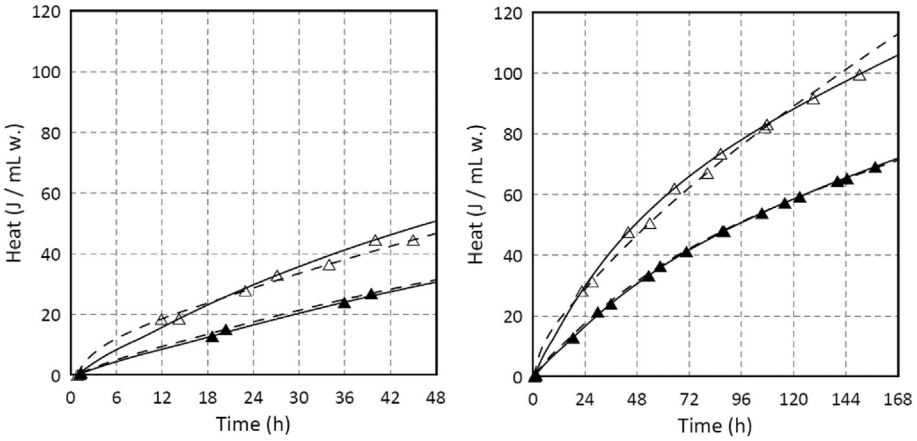

Fig. 8. Calorimetry results (total normalized heat released over time) for pastes produced with materials annealed at higher temperatures (~860 °C).

Regression coefficients for LOI, heat of hydration and strength response models are shown in Table 5. As seen in Fig. 4, increasing annealing temperature increases the LOI of the materials. LOI also increases with increasing residence times. Although not satisfying the significance criterion selected, the interaction between annealing temperature and residence time (X1:X2, p-value 0.1018) deserves attention. As a result of this interaction, the effect of residence time would be larger at lower temperatures and smaller in the opposite case. This can be expected if the rate of dehydration of the C-S-H increases with increasing temperature. At lower temperatures the dehydrated fraction will be limited by the residence time, whereas at higher temperatures the dehydrated fraction might be limited by the availability of water or other volatiles. Accordingly, residence time would be a critical parameter to control the fraction of relevant phases formed at lower temperatures.

Total heat released over 24 h and over 7 days of hydration was significantly affected by the annealing temperature used to obtain the reactivated materials (Figs. 5 and 6). Materials obtained at lower annealing temperatures released larger total heat over 24 h as well as over 7 days, indicating higher reactivity. According to the regression of the results, both for 24-hour and 7-day heat release, increasing annealing temperature significantly decreases the reactivity (total heat released over time) of the reactivated materials. Largest regression coefficients below that of annealing temperature are the residence time (for 7-day heat) and the interaction of residence time and annealing temperature (for both 24-hour and 7-day heat). According to these coefficients, the effect of residence time on the reactivity of the materials depends on the annealing temperature. However, as seen in Figs. 5 and 6, these effects are probably an artifact of small differences in annealing temperature in the high temperature cases (~860 °C). In Fig. 5, the results for the low temperature group of cases (~740 °C) seem to confirm that at lower

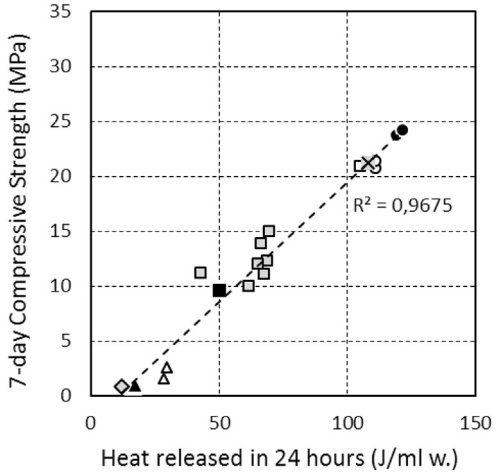

Fig. 9. 7-day compressive strength versus 24-hour normalized heat release of reactivated material pastes.

annealing temperatures increasing residence time increases initial (24 h) reactivity of the materials, whereas the opposite is observed for the central cases at a higher annealing temperature. After 7 days however, as seen in Fig. 6, at lower annealing temperatures residence time had no effect on total heat released. This behavior can also be seen in the isothermal calorimetry curves from 0 to 48 h and from 0 to 168 h for materials annealed at ~740 °C (Fig. 7) and at ~860 °C (Fig. 8). In addition, within the group annealed at ~860 °C for short residence times, a small increase in total heat release over 7 days was observed for the material that underwent a slower cooling rate (Fig. 8).

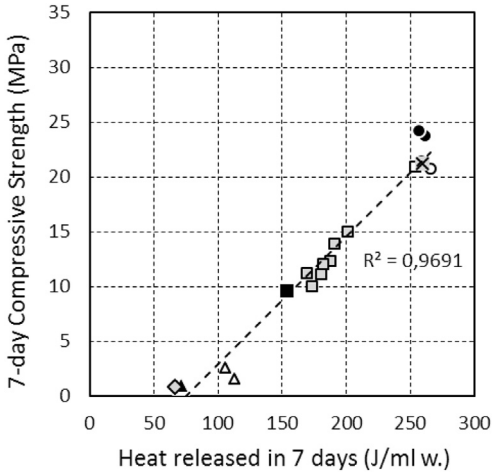

Fig. 10. 7-day compressive strength versus 7-day normalized heat release of reactivated material pastes.

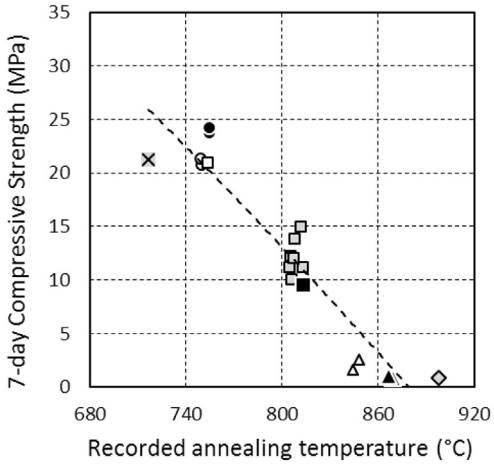

Fig. 11. 7-day compressive strength versus annealing temperature of reactivated material.

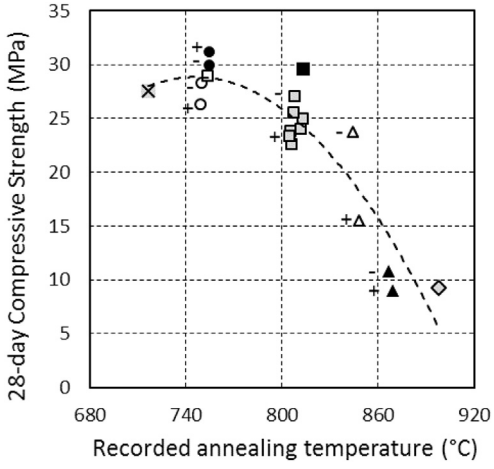

Fig. 12. 28-day compressive strength versus annealing temperature of reactivated material.

Results for 7-day strength of reactivated material pastes show a strong linear correlation with the normalized heat released by the pastes both over 24 h and over 7 days (Figs. 9 and 10). Therefore, isothermal calorimetry appears as a reliable method to continuously monitor early-age strength development in reactivated materials.

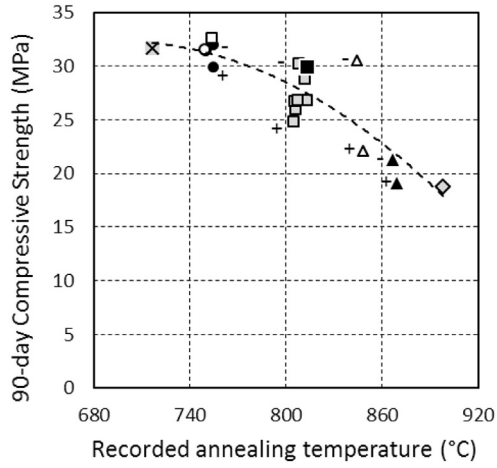

Fig. 13. 90-day compressive strength versus annealing temperature of reactivated material.

Moreover, as seen in Fig. 9, a short − 24 h-calorimetry measurement could be used to predict 7-day strength. At later ages however, the strength gain of the reactivated material pastes deviate from the early age calorimetry results. Just as in the case of heat release, the regression of 7-day strength results indicates annealing temperature is the only factor having a significant effect on the response. In the region explored, increasing annealing temperature significantly decreases 7-day compressive strength (Fig. 11). However, regression of 28-day and 90-day strength results show increasingly significant effects of residence time and cooling rate, as well as significant interaction and second order effects (Table 5). As seen in Figs. 12 and 13, and also according to the regression of results, the effect of residence time depends on the annealing temperature. At higher annealing temperatures, increasing residence time decreases 28-day strength, whereas at lower annealing temperatures the opposite is observed. This is only partly explained by the differences in annealing temperature between short- and long-residence time cases within the high temperature group (846 °C versus 868 °C, respectively) since, even when adjusting by the general trend of strength-temperature, the difference is significant. As seen in Fig. 13, at 90-days the effect of residence time on strength remains evident only at higher annealing temperatures, decreasing strength as residence time increases. Although according to the regression the main effect of residence time is stronger on 90-day strength, at lower annealing temperatures it is neutralized by the interaction effect with annealing temperature. The small but significant second order coefficient for the effect of residence time predicts lower strengths are achieved at the central level of the residence time (90 min). However, this is probably an artifact of the regression due to the temperature difference of the B_14 case.

As seen in Figs. 12 and 13, the strength results display a marked non-linear relation to annealing temperature level. Regression of results indicate annealing temperature has a significant second order effect on 28-day strength (almost significant on 90-day strength). This marked curvature of the response is consistent with the existence of an optimal annealing temperature as reported in previous studies [6,8,33]. However, the shape of the factor-response relationship between annealing temperature and strength cannot be properly fitted with just a second order model. Most likely, the effect of annealing temperature involves several phenomena that overlap to shape the observed response, such as the varying concentration and microstructural characteristics of the reactive phases formed in the materials at different temperatures as is discussed in the next subsection. Nevertheless, results indicate short- and long-term strength could be optimized simultaneously, i.e. processing the hydrated precursor material at a unique annealing temperature. In fact, higher short- and long-term strengths were recorded

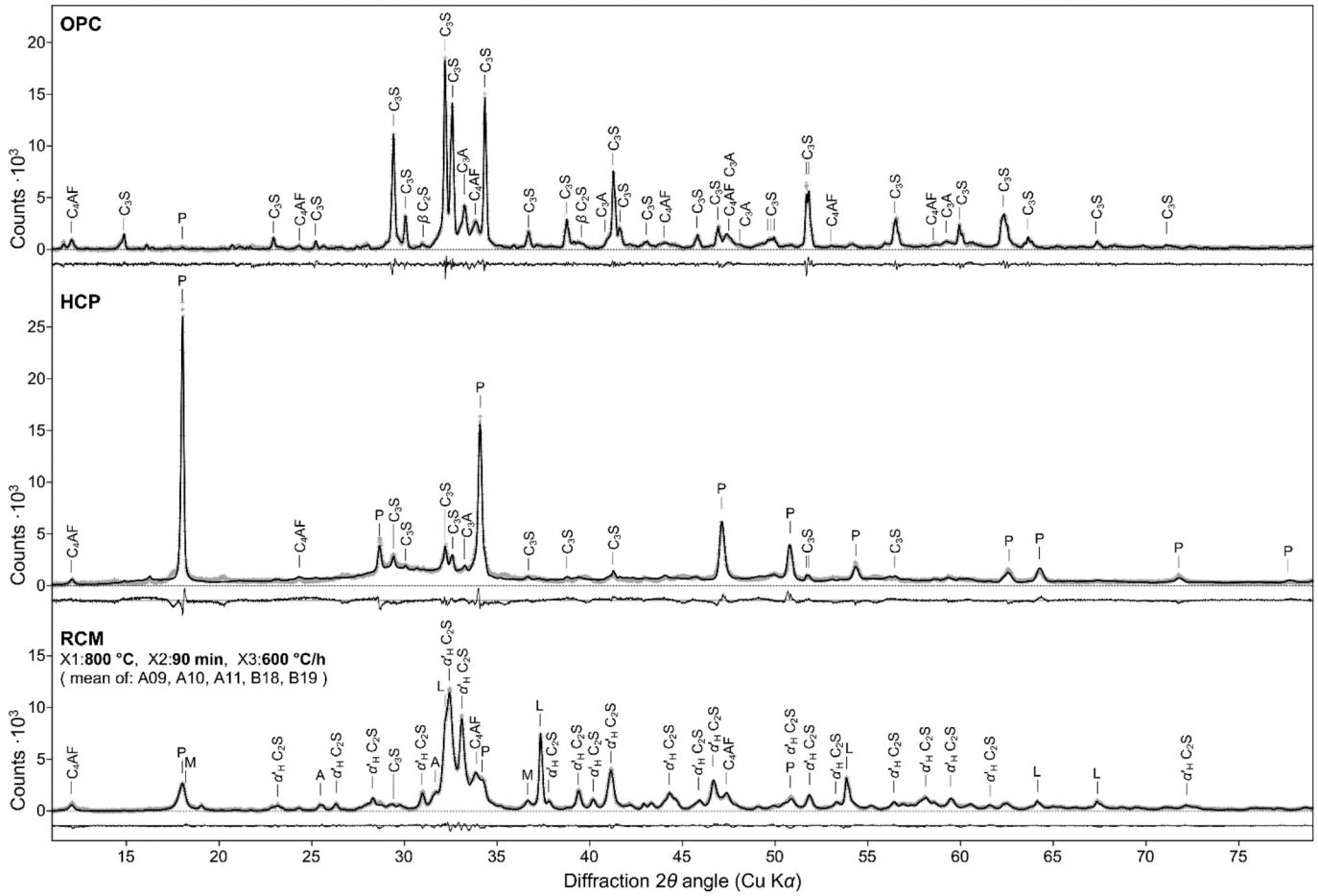

Fig. 14. Diffractograms used for initial refinement of the crystal structures for the quantitative analysis: Experimental, calculated (Rietveld) and residual (calculated–experimental) XRD profiles of the Portland cement (OPC), the hydrated cement paste (HCP) obtained from it (precursor material) and the reactivated cementitious material (RCM) obtained at the central case of the experimental design (800 °C annealing temperature, 90 min residence time, 600 °C/h cooling rate, average of 5 replications). Main peaks from principal identified phases are marked: C_3S: monoclinic tri-calcium silicate, α'_H C_2S, β C_2S and γ C_2S: alpha′$_H$, beta and gamma di-calcium silicate polymorphs, respectively, C_3A: tri-calcium aluminate, C_4AF: tetra-calcium alumino-ferrite, L: free lime (CaO), P: Portlandite ($Ca(OH)_2$), A: Anhidrite ($CaSO_4$), M: Mayenite ($Ca1_2Al_{14}O_{33}$).

for materials annealed at around 750 °C, although the strength of specific cases also depended on the residence time applied. The dependence is consistent with the significant interaction effect between of both factors identified in the regression of results. According to the response models for 28-day and 90-day strength, the optimal annealing temperature would be higher when shorter residence times are used and lower in the opposite case. However, due to the independent effect of residence time, the optimal strength achieved would be higher at the low-temperature and long-residence-time combination. Finally, as also seen in Figs. 11, 12 and 13, cooling rate affected 28-day and 90-day strength of materials annealed at higher temperatures. Regression of results for 28-day and 90-day strength indicate fast cooling rates have a negative effect on the strength of reactivated material pastes, particularly at 90 days of age. This effect is probably larger at higher annealing temperatures judging by the relatively large (although not significant) coefficient of the temperature and cooling rate interaction on 90-day strength.

In addition to exhibiting higher strengths at all ages measured, the initial strength gain rate of materials annealed at lower temperatures was also much higher than that of materials annealed at higher temperatures. At 7 days of hydration materials annealed at around 740 °C on average achieved > 70% of their respective 90-day strength, whereas at the same age materials annealed at around 860 °C on average achieved < 7% of their respective 90-day strength. The strength difference between the two groups decreased over time. Nevertheless, at 90 days of hydration the high temperature group still lagged behind, achieving on average 74.5% of the average strength achieved by the lower temperature group.

3.2. Quantitative XRD analysis of reactivated materials

According to the analysis of the XRD data, the phase composition of the reactivated materials vary widely across the experimental region explored. Alpha′$_H$ and beta polymorphs of C_2S, Lime (CaO), Portlandite ($Ca(OH)_2$), Mayenite ($Ca_{12}Al_{14}O_{33}$), and major constituent phases of the original cement were identified in all the reactivated materials (Fig. 14). In addition, depending on annealing temperature, gamma-C_2S, Anhydrite ($CaSO_4$) and a mineral with a pattern matching that of Ternesite ($Ca_5(SiO_4)2SO_4$), were also identified. Alpha′$_L$-C_2S was not detected in the reactivated materials. In the quantification results the concentrations of Lime and Portlandite were observed to inversely correlate. Considering the materials were obtained at temperatures exceeding 700 °C, it was assumed that Portlandite present was the result of partial hydration of Lime due to exposure to ambient humidity. Accordingly, the CaO part of the Portlandite fraction (i.e. the refined weight fraction of Portlandite by the ratio of molar masses: $m_{CaO}/m_{Ca(OH)2}$) was added to the Lime fraction and quantification results were normalized to the calculated total ignited mass, as in:

$$W_i = \frac{w_i}{1 - w_{Portlandite}(m_{H_2O}/m_{Ca(OH)_2})} \quad (1)$$

where, W_i is the normalized weight fraction of phase i, w_i is its refined

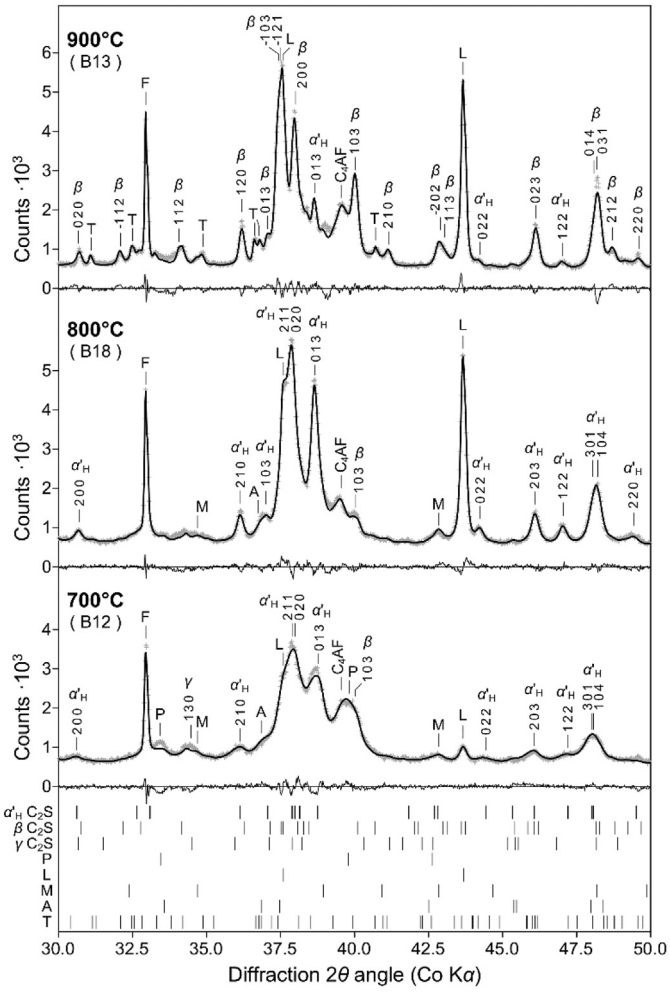

Fig. 15. Experimental, calculated (Rietveld) and residual (calculated–experimental) XRD profiles of reactivated materials obtained over the full range of annealing temperatures explored (~700 °C, 800 °C and ~900 °C, cases B_12, B_18 and B_13, respectively) at fixed residence time (90 min) and cooling rate (600 °C/h). Main peaks of principal phases identified are marked above the profiles: α'_H, β and γ: alpha'$_H$, beta and gamma di-calcium silicate polymorphs, respectively, C_4AF: tetra-calcium alumino-ferrite, P: Portlandite ($Ca(OH)_2$), L: free lime (CaO), M: Mayenite ($Ca1_2Al_{14}O_{33}$), A: Anhidrite ($CaSO_4$), T: Ternesite ($Ca_5(SiO_4)2SO_4$). Di-calcium silicate peaks include Laue indices of diffraction contributing planes.

weight fraction, $w_{Portlandite}$ is the refined weight fraction of Portlandite and m_{H_2O} and $m_{Ca(OH)_2}$ are the molar masses of Lime and Portlandite, respectively. Unfortunately, the presence of Portlandite complicates the use of the internal standard for the normalization of phase weight fractions. If some hydration has occurred in the materials before or during the intermixing of the internal standard, the ratio of standard to ignited mass cannot be accurately determined. Consequently, in the following discussion, and in the tables and figures that accompany it, the quantification results are presented as percent fractions of the total ignited mass of crystalline phases identified excluding the internal standard. Nevertheless, an estimation of the explained fraction (i.e. the fraction of the sample mass identified and quantified in the refinement) is presented in Table 6, based on the ratio of intermixed fraction of the standard to its refined fraction.

As shown in Table 6, according to the QXRD analysis, C_2S polymorphs, constituent phases of the original cement and free Lime contribute the largest portion to the crystalline phases present in the reactivated materials. In total, the fraction comprised by the sum of cement phases and Lime accounts for around 38% of the mass on average, and remains relatively constant across the experimental design. Likewise, the sum of C_2S polymorphs remains relatively constant and accounts for around 52% of the mass on average. However, the relative concentration of each polymorph within the group is seen to vary widely across the experiment. The relative contribution of alpha'$_H$- and beta-C_2S at their refined fractions to the calculated XRD profile for cases B_12 (~700 °C), B_18 (~800 °C) and B_13 (~900 °C) can be seen in Fig. 15. The relationship between annealing temperature and refined weight fractions obtained for each C_2S polymorph in the reactive materials is presented in Fig. 16. In the range of temperatures explored, the refined fractions of all the C_2S polymorphs are highly dependent on annealing temperature. The refined fractions of alpha'$_H$- and gamma-C_2S decrease with increasing temperature, whereas the refined fraction of beta-C_2S increases with increasing temperature. Consequently, in materials produced at lower annealing temperatures the fraction of alpha'$_H$-C_2S exceeds that of beta-C_2S, whereas in materials obtained at higher temperatures the opposite is observed. In addition, gamma-C_2S is not detected in materials annealed above 800 °C. The observed correlations are expected since all these phases are products of a common precursor material. Results indicate gamma-C_2S might be forming first, and then transforming directly to alpha'$_H$-C_2S (considering the complete absence of alpha'$_L$-C_2S). Regardless of whether gamma-C_2S is forming as an intermediate phase, these results show that starting from C-S-H alpha'$_H$-C_2S forms at much lower temperatures compared to those reported for when starting from gamma-C_2S via alpha'$_L$-C_2S

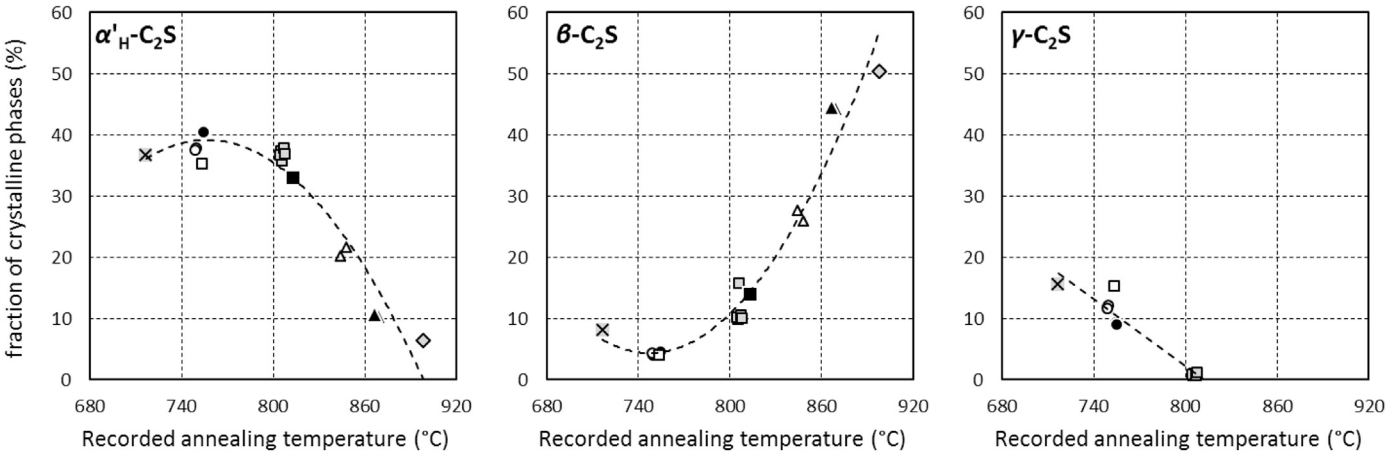

Fig. 16. Refined weight fractions of C_2S polymorphs versus annealing temperature.

Table 6
Quantification of crystalline phases in reactivated materials (Rietveld method).

ID	Rietveld refinement		Internal std. CaF2		Refined weight fractions of crystalline phases identified (not including internal standard)													Explained fraction
					Original cement constituents					C_2S Polymorphs				Other				
	Sigma	R_{wp} (%)	Mix (%)	Refined (%)	C_3S (%)	C_4AF (%)	C_3A (%)	P[a] (%)	Total (%)	α'_H (%)	β (%)	γ (%)	Total (%)	Lime (%)	M[a] (%)	T[a] (%)	A[a] (%)	
A_01	1.37	4.51	5.167	7.6	3.9	6.8	2.0	0.9	13.6	37.7	3.9	12.0	53.6	23.6	6.8		2.5	0.683
A_02	1.44	4.77	5.006	6.4	3.0	12.3	1.7	1.3	18.3	20.1	27.6		47.7	21.6	5.6	6.3	0.5	0.785
A_03	1.35	4.48	5.036	7.7	3.3	8.1	1.5	1.1	14.0	40.4	4.8	9.4	54.5	22.8	6.0		2.7	0.654
A_04	1.48	4.97	5.222	7.0	1.8	11.3	0.9	1.0	15.0	10.6	44.5		55.1	18.7	4.6	6.5		0.747
A_05	1.32	4.36	5.010	8.8	3.9	6.7	2.8	1.0	14.4	37.5	4.3	11.6	53.4	21.5	8.0		2.8	0.570
A_06	1.55	5.13	4.788	6.8	3.1	12.9	1.3	1.1	18.3	21.6	25.8		47.4	22.4	6.0	5.3	0.6	0.704
A_07	1.33	4.35	5.419	9.4	3.2	7.7	1.8	1.1	13.8	40.5	4.6	9.1	54.2	23.2	6.6		2.2	0.576
A_08	1.50	4.90	5.047	6.7	1.6	11.7	0.9	1.3	15.5	10.3	44.2		54.5	19.0	5.1	5.9		0.758
A_10	1.42	4.85	5.112	7.4	3.1	11.1	2.1	1.1	17.4	35.6	15.7	0.9	52.2	20.4	5.7	2.3	2.1	0.682
A_11	1.43	4.71	5.142	8.9	4.1	11.7	1.7	1.0	18.5	37.3	9.8	0.7	47.8	23.5	6.4	1.7	2.1	0.574
B_12	1.34	4.61	4.864	7.1	3.4	5.6	3.4	0.9	13.3	36.6	8.1	15.5	60.2	20.5	3.4		2.7	0.696
B_13	1.53	5.22	5.156	6.1	1.3	12.1	0.9	1.2	15.5	6.3	50.3		56.6	17.0	4.9	6.0		0.846
B_14	1.56	5.29	4.999	7.9	4.8	6.5	2.8	0.8	14.9	35.2	3.9	15.2	54.3	22.0	5.8		2.9	0.631
B_15	1.45	4.84	5.072	8.0	4.2	12.3	1.7	1.2	19.3	33.0	13.9		47.0	23.1	6.9	1.9	1.8	0.635
B_16	1.41	4.63	4.872	7.9	3.0	11.2	2.5	1.1	17.8	36.8	10.0	1.0	47.9	22.1	7.9	2.1	2.2	0.614
B_17	1.46	4.81	4.809	7.9	3.7	11.8	2.0	1.0	18.6	36.7	10.1	0.7	47.5	23.0	7.1	2.0	1.9	0.610
B_18	1.42	4.73	4.780	7.2	3.7	11.1	1.9	1.1	17.7	37.8	10.4	0.6	48.8	23.3	6.2	1.9	2.1	0.673
Min.	1.32								13.3	6.3	3.9		47.3	17.0				0.570
Mean	1.43								16.2	30.2	17.2		51.9	21.6				0.672
Max.	1.56								19.2	40.5	50.3		60.2	23.6				0.846
Standard deviation across experiment (fraction of mean)									0.13				0.13	0.09				0.117

[a] P: Periclase, M: Mayenite, T: Ternesite, A: Anhydrite.

(alpha′$_L$ to alpha′$_H$: 1160 °C [5,34]). This much lower temperature of formation is expected when the reactants are mixed on a much smaller scale prior to the thermal process, which would be the case when the precursor material is a nearly amorphous hydrated calcium silicate [35] or a sol-gel as in the Pechini process [36,37].

Refinement results for the crystallite sizes of the C_2S polymorphs (Table 7) provide a plausible explanation for the presence of large fractions of stable alpha′$_H$-C_2S at room temperature in the reactivated materials produced at lower temperatures. As can be seen in Fig. 17, the refined crystallite size of all C_2S polymorphs in the reactivated materials increases with increasing annealing temperature. Notably, the refined crystallite sizes of the different polymorphs at similar temperatures are comparable, meaning they depend mostly on annealing temperature and not on the crystal structure of the polymorph. Since formation of C_2S from the finely divided dehydrating C-S-H is a sintering process, grain growth is controlled by temperature. Due to their smaller crystallite sizes, C_2S polymorphs formed at lower temperatures are expected to have much higher surface areas. A high surface area is known to prevent the transformation of high temperature polymorphs to more stable phases on cooling [38]. Assuming alpha′$_H$-C_2S forms directly from C-S-H (or from gamma-C_2S formed from C-S-H), in materials annealed at lower temperatures its transformation to beta-C_2S on cooling is restricted by the high surface area associated with its small crystallite size. As annealing temperature is increased, the resulting surface area decreases and progressively more alpha′$_H$-C_2S is able to transform to beta-C_2S on cooling. This explains why in the range explored, as annealing temperature is increased the concentration of alpha′$_H$-C_2S in the reactivated material decreases, that of beta-C_2S increases, and the overall fraction of C_2S remains fairly constant.

An additional consequence of the higher surface area associated with a smaller crystallite size is an increased reactivity due to the effect of surface area on the water solubility of C_2S [37]. This effect adds on to

Table 7
QXRD-adjusted crystal structure model parameters (Rietveld refinement). Values in italics correspond to those found in the reference structure (not refined).

ID	α'_H-C_2S					β-C_2S						γ-C_2S		Lime	
	Fraction (%)	*a* (Å)	*b* (Å)	*c* (Å)	c. size (Å)	Fraction (%)	*a* (Å)	*b* (Å)	*c* (Å)	β (°)	c. size (Å)	Fraction (%)	c. size (Å)	Fraction (%)	c. size (Å)
A_01	37.7	6.7896	5.5111	9.3082	242	3.9						12.0	202	23.6	960
A_02	20.1	6.7616	5.5386	9.2990	1045	27.6	5.5162	6.7654	9.3222	94.32	1266			21.6	1414
A_03	40.4	6.7845	5.5134	9.3076	275	4.8						9.4	264	22.8	1133
A_04	10.6	6.7591	5.5410	9.2962	919	44.5	5.5156	6.7638	9.3218	94.36	1224			18.7	1477
A_05	37.5	6.7892	5.5106	9.3076	237	4.3						11.6	211	21.5	1137
A_06	21.6	6.7607	5.5371	9.3006	955	25.8	5.5156	6.7675	9.3271	94.32	1357			22.4	1754
A_07	40.5	6.7851	5.5129	9.3093	269	4.6						9.1	289	23.2	1298
A_08	10.3	6.7600	5.5370	9.3000	1049	44.2	5.5151	6.7638	9.3214	94.36	1191			19.0	2090
A_10	35.6	6.7658	5.5333	9.3020	562	15.7	5.5171	6.7696	9.3216	*94.30*	612	0.9		20.4	1243
A_11	37.3	6.7656	5.5296	9.3026	529	9.8	5.5158	6.7646	9.3213	*94.30*	913	0.7		23.5	1481
B_12	36.6	6.7982	5.5126	9.3069	214	8.1						15.5	162	20.5	729
B_13	6.3	6.7570	5.5401	9.2992	1454	50.3	5.5158	6.7646	9.3213	94.38	1096			17.0	1931
B_14	35.2	6.7898	5.5073	9.3067	216	3.9						15.2	189	22.0	866
B_15	33.0	6.7611	5.5350	9.3004	684	13.9	5.5176	6.7676	9.3275	94.27	943			23.1	1419
B_16	36.8	6.7643	5.5323	9.3051	566	10.0						1.0		22.1	1408
B_17	36.7	6.7642	5.5324	9.3052	573	10.1						0.7		23.0	1617
B_18	37.8	6.7653	5.5316	9.3026	540	10.4	5.5154	6.7808	9.3251	*94.30*	686	0.6		23.3	1255

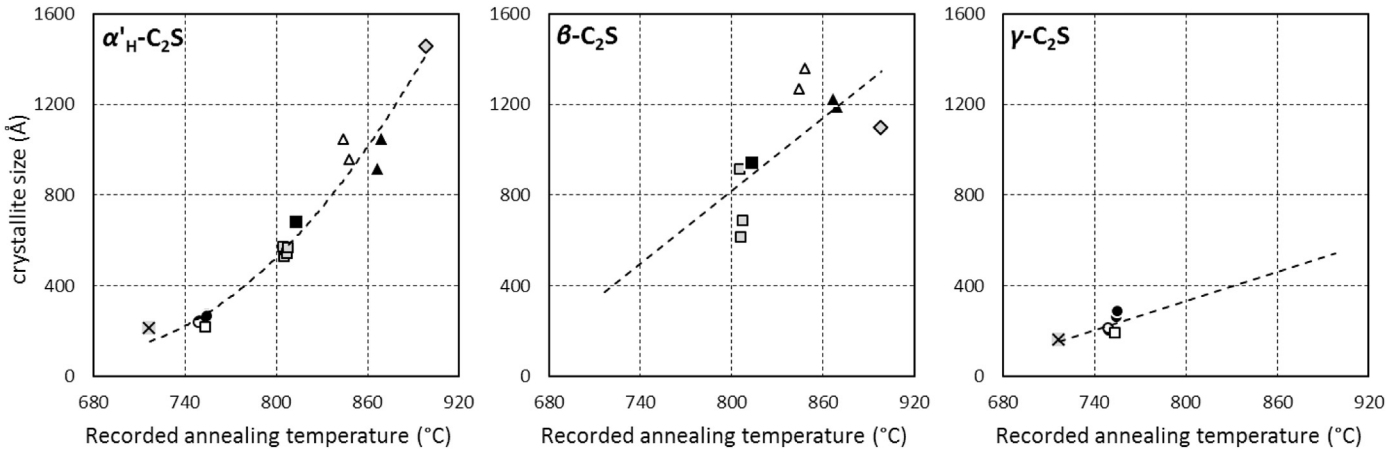

Fig. 17. Refined crystallite sizes of C_2S polymorphs versus annealing temperature.

the intrinsic higher reactivity of alpha′$_H$- compared to beta-C_2S, and contribute to explain the differences in heat of hydration and strength gain rate between the reactivated material pastes. In the results from the refinement of the crystallite size of C_2S polymorphs it is not possible to isolate the effects of residence time and cooling rate. Nevertheless, the XRD profiles of materials obtained applying different residence times at the same annealing temperature and cooled at the same rate do show diffraction peaks thinning as residence time increases (Fig. 18). Similarly, for free Lime, refinement results indicate that crystallite size increases with increasing residence time and with increasing cooling rates (Fig. 19). Most free Lime in the reactivated materials is expected to form during the heating of the precursor material by dehydration of Portlandite. In fact, a marked decrease in heating rate related to the endotherm of Portlandite dehydration was observed at around 550 °C in the material temperature recorded during the heating process. Nevertheless, if residence time has a similar effect on the crystallite size of alpha′$_H$-C_2S, its negative effect on the reactivity of the material is compensated by the larger fraction of the phase formed after a longer residence time. As seen in Fig. 16, in reactivated materials obtained at ~740 °C, the refined fraction of alpha′$_H$-C_2S appears to increase with increasing residence time, while the refined fraction of gamma-C_2S decreases.

Refinement of lattice parameters indicate that the crystal structure of alpha′$_H$-C_2S present in the reactivated materials is significantly affected by the annealing temperature used. The largest deviation from the average value of sizes *a* and *b* was found in reactivated materials obtained at lower annealing temperatures (Fig. 20), where the refined fraction of alpha′$_H$-C_2S is also largest. Despite the change in dimensions, the average deviation between calculated unit cell volumes at different annealing temperatures is < 0.05% (maximum deviation 0.16%). The deformed structure observed in the materials annealed at low temperature is probably related to the large ratio of surface area to internal volume in the small crystallites present in these materials. The refinement of lattice parameters for beta-C_2S showed less variation across the temperature range. However, this can only be said for materials obtained at annealing temperatures at or above 800 °C since strong overlap of main peaks of alpha′$_H$ and beta-C_2S prevented refinement of lattice parameter and crystallite sizes of beta-C_2S in the materials obtained at lower temperatures.

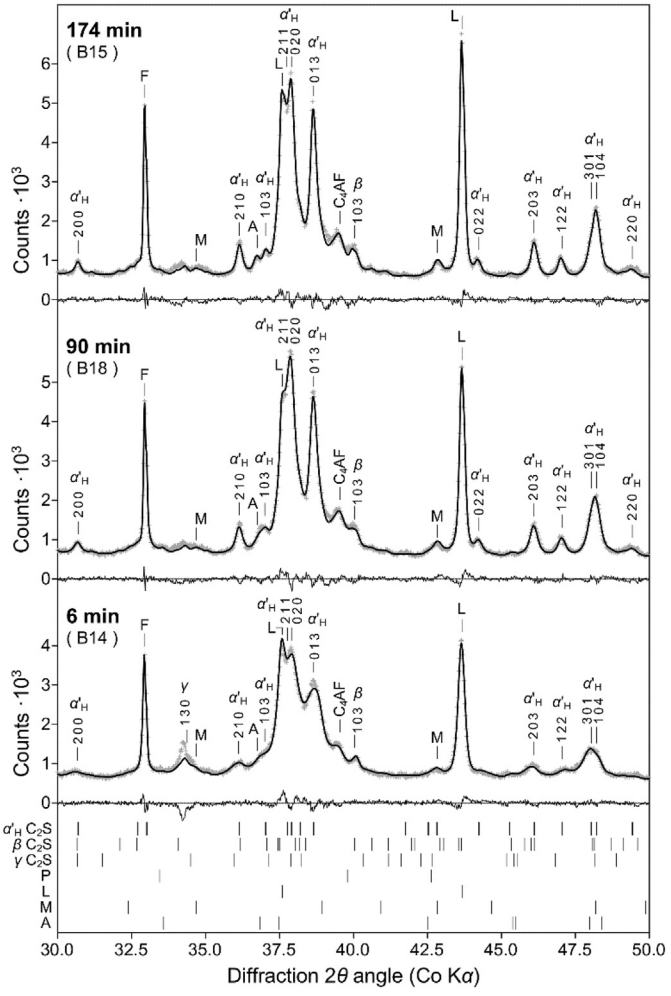

Fig. 18. Experimental, calculated (Rietveld) and residual (calculated–experimental) XRD profiles of reactivated materials obtained over the full range of residence times explored (6 min, 90 min and 174 min, cases B_14, B_18 and B_15, respectively) at fixed annealing temperature (800 °C) and cooling rate (600 °C/h). Main peaks of principal phases identified are marked above the profiles: α'_H, β and γ: alpha′$_H$, beta and gamma di-calcium silicate polymorphs, respectively, C_4AF: tetra-calcium alumino-ferrite, P: Portlandite ($Ca(OH)_2$), L: free lime (CaO), M: Mayenite ($Ca12Al_{14}O_{33}$), A: Anhidrite ($CaSO_4$). Di-calcium silicate peaks include Laue indices of diffraction contributing planes.

4. Conclusions

As shown in the reported study using quantitative analysis of X-ray diffraction data, the hydration reactivity and subsequent mechanical

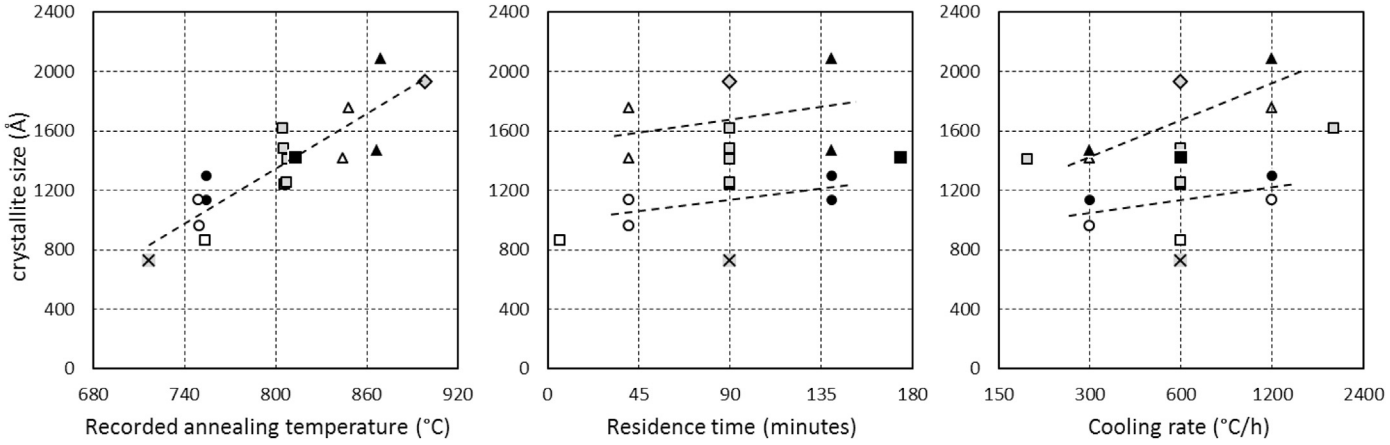

Fig. 19. Effect of thermal parameters on the refined crystallite size of CaO.

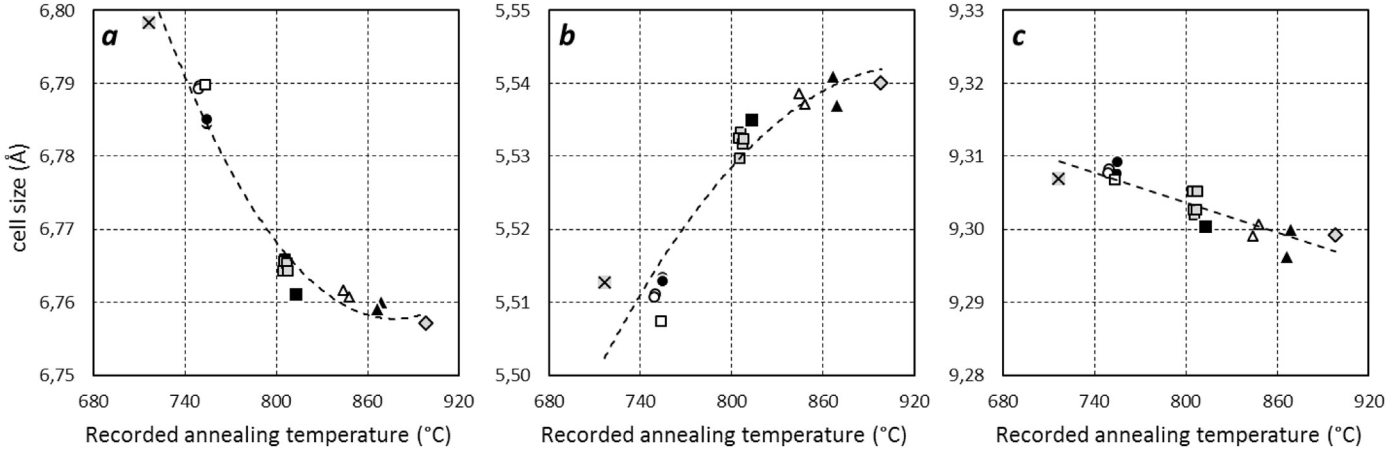

Fig. 20. Effect of annealing temperature on the refined lattice parameters of alpha′$_H$-C_2S.

properties of the recycled cementitious materials obtained by thermal processing of hydrated cement pastes is explained by the relative concentration and microstructural characteristics of alpha′$_H$-C_2S and beta-C_2S in them. These, in turn, depend on the parameters of the thermal process applied. In this study, annealing temperature, residence time and cooling rate were all found to affect the observed responses, although in decreasing order of impact. When starting from the calcium silicate hydrate present in the hardened cement paste, alpha′$_H$-C_2S forms at lower temperatures than those reported for when it is formed from clinker raw materials or other C_2S polymorphs. Subsequent stability on cooling of the alpha′$_H$-C_2S formed from calcium silicate hydrates is highly dependent on annealing temperature due to the effect of temperature on its crystallite size. A larger fraction of the alpha′$_H$-C_2S formed remains stable on cooling in materials annealed at lower temperature due their smaller crystallite size. Due to the finite rate of formation, linked to the rate of decomposition of the calcium silicate hydrates, the concentration of alpha′$_H$-C_2S is also dependent on the combination of annealing temperature and residence time. In concordance with the above, annealing temperature is the parameter having the largest effect on the heat of hydration and on the 7, 28 and 90-day strength of reactivated material pastes. According to response models obtained from regression of experimental results obtained in this study, in the range of annealing temperatures explored higher strengths are achieved by pastes made with materials obtained at lower temperatures. Also in line with the above, the response models for 28-day and 90-day strength show that the effect of annealing temperature is not linear, predicting an optimal response around 740 °C, and provide evidence for a significant interaction effect between residence time and annealing temperature. Considering the evolution of strength over time, it can be concluded that materials obtained at temperatures around 740 °C achieved higher early-age strengths due to higher initial strength gain rate. Cooling rate had a smaller effect on the responses, although increasing in significance at later hydration ages. Within materials obtained at higher temperatures, higher strengths were achieved by those subject to lower cooling rates.

Results from quantitative analysis of X-ray diffraction data by the Rietveld method provided explanations for the observed effects of thermal process parameters on the reactivity and mechanical behavior of the materials. The higher strength gain rate observed in materials obtained at lower temperatures is a result of their higher relative concentration of alpha′$_H$-C_2S, compared to the less reactive beta-C_2S and of the higher reactivity of both phases that results from a smaller average crystallite size (higher surface areas). Even though the total concentration of reactive C_2S polymorphs was found to be approximately constant in materials obtained across the range of annealing temperatures, at 90 days of hydration the strength of pastes made with materials obtained at higher temperatures still lags behind those obtained at lower temperatures. In addition to beta C_2S being less reactive, the strength gain of materials obtained at higher temperatures is negatively affected by the lower reactivity arising from the larger crystallite size of the phases formed in them. Neither results from quantification of phases nor crystallite size provided definitive explanation for the effect of cooling rate on the strength of the reactive material pastes. However, considering crystallite size of Lime increases with increasing cooling rate, a similar phenomenon might be affecting the reactive polymorphs of C_2S, although beyond the detection limits of the analysis implemented in this study.

Acknowledgments

We acknowledge support from the Chilean National Commission for Scientific and Technological Research, CONICYT, through FONDECYT project 11140675. We express our gratitude to Professor Pablo Pastén of the Department of Hydraulic and Environmental Engineering, Mr. Patricio Pérez from the Metallurgy Laboratory of the Department of Mechanical and Metallurgical Engineering, and Mr. Mauricio Guerra from the Construction Materials Laboratory of the Department of Construction Engineering and Management, all from the School of Engineering of Pontificia Universidad Católica de Chile at Santiago.

References

[1] E. Gartner, H. Hirao, A review of alternative approaches to the reduction of CO_2 emissions associated with the manufacture of the binder phase in concrete, Cem. Concr. Res. 78 (2015) 126–142.
[2] D. Gastaldi, F. Canonico, L. Capelli, L. Buzzi, E. Boccaleri, S. Irico, An investigation on the recycling of hydrated cement from concrete demolition waste, Cem. Concr. Compos. 61 (2015) 29–35, http://dx.doi.org/10.1016/j.cemconcomp.2015.04.010.
[3] J. Schoon, K. De Buysser, I. Van Driessche, N. De Belie, Fines extracted from recycled concrete as alternative raw material for Portland cement clinker production, Cem. Concr. Compos. 58 (2015) 70–80, http://dx.doi.org/10.1016/j.cemconcomp.2015.01.003.
[4] M. Fridrichová, Hydration of belite cements prepared from recycled concrete residues, Ceramics-Silikaty 51 (2007) 45–51.
[5] H.F.W. Taylor, Cement Chemistry, 2nd ed., Thomas Telford, London, 1997.
[6] R. Serpell, M. Lopez, Properties of mortars produced with reactivated cementitious materials, Cem. Concr. Compos. 64 (2015), http://dx.doi.org/10.1016/j.cemconcomp.2015.08.003.
[7] Z. Shui, D. Xuan, W. Chen, R. Yu, R. Zhang, Cementitious characteristics of hydrated cement paste subjected to various dehydration temperatures, Constr. Build. Mater. 23 (2009) 531–537, http://dx.doi.org/10.1016/j.conbuildmat.2007.10.016.
[8] R. Serpell, M. Lopez, Reactivated cementitious materials from hydrated cement paste wastes, Cem. Concr. Compos. 39 (2013), http://dx.doi.org/10.1016/j.cemconcomp.2013.03.020.
[9] H.M. Rietveld, A profile refinement method for nuclear and magnetic structures, J. Appl. Crystallogr. 2 (1969) 65–71.
[10] G.E.P. Box, K.B. Wilson, On the experimental attainment of optimum conditions, J. R. Stat. Soc. Ser. B (Stat Methodol.) 13 (1951) 1–45.
[11] G. Walenta, T. Füllmann, Advances in quantitative XRD analysis for clinker, cements, and cementitious additions, Adv. X-ray Anal. 47 (2004) 287–296.
[12] R. Snellings, A. Bazzoni, K. Scrivener, The existence of amorphous phase in Portland cements: physical factors affecting Rietveld quantitative phase analysis, Cem. Concr. Res. 59 (2014) 139–146, http://dx.doi.org/10.1016/j.cemconres.2014.03.002.
[13] National Institute of Standards and Technology—NIST, Materials and Structural Systems Division, GSAS Tutor.—Files, (2015).
[14] S. Grazulis, D. Chateigner, R.T. Downs, A.T. Yokochi, M. Quiros, L. Lutterotti, et al., Crystallography open database—an open-access collection of crystal structures, J. Appl. Crystallogr. 42 (2009) 726–729, http://dx.doi.org/10.1107/S0021889809016690.
[15] G. Le Saoût, V. Kocaba, K. Scrivener, Application of the Rietveld method to the analysis of anhydrous cement, Cem. Concr. Res. 41 (2011) 133–148, http://dx.doi.org/10.1016/j.cemconres.2010.10.003.
[16] L. Lutterotti, Total pattern fitting for the combined size-strain-stress-texture determination in thin film diffraction, Nucl. Inst. Methods Phys. Res. B (2010) 334–340.
[17] A.G. De la Torre, S. Bruque, J. Campo, M.A.G. Aranda, The superstructure of C_3S from synchrotron and neutron powder diffraction and its role in quantitative phase analyses, Cem. Concr. Res. 32 (2002) 1347–1356, http://dx.doi.org/10.1016/S0008-8846(02)00796-2.
[18] W.G. Mumme, R.J. Hill, G. Bushnell-Wye, E.R. Segnit, Rietveld crystal structure refinements, crystal chemistry and calculated powder diffraction data for the polymorphs of dicalcium silicate and related phases, Neues Jahrb. Fuer Mineral. Abhandlungen. 169 (1995) 35–68.
[19] R. Berliner, C. Ball, P.B. West, Neutron powder diffraction investigation of model cement compounds, Cem. Concr. Res. 27 (1997) 551–575, http://dx.doi.org/10.1016/S0008-8846(97)00028-8.
[20] R.W.G. Wyckoff, Crystal Structures 1, 2nd ed., Wiley, New York, 1963.
[21] L. Desgranges, D. Grebille, G. Calvarin, G. Chevrier, N. Floquet, J.-C. Niepce, et al., Hydrogen thermal motion in calcium hydroxide: $Ca(OH)_2$, Acta Crystallogr. Sect. B: Struct. Sci. 49 (1993) 812–817, http://dx.doi.org/10.1107/S0108768193003556.
[22] H. Effenberger, K. Mereiter, J. Zemann, Crystal structure refinements of magnesite, calcite, rhodochrosite, siderite, smithonite, and dolomite, with discussion of some aspects of the stereochemistry of calcite type carbonates, Zeitschrift Für Krist. - Cryst. Mater. 156 (1981) 233–243, http://dx.doi.org/10.1524/zkri.1981.156.3-4.233.
[23] W.F. Cole, C.J. Lancucki, A refinement of the crystal structure of gypsum $CaSO_4{\cdot}2H_2O$, Acta Crystallogr. Sect. B: Struct. Crystallogr. Cryst. Chem. 30 (1974) 921–929, http://dx.doi.org/10.1107/S0567740874004055.
[24] P. Ballirano, A. Maras, S. Meloni, R. Caminiti, The monoclinic I2 structure of bassanite, calcium sulphate hemihydrate ($CaSO_4{\cdot}0.5H_2O$), Eur. J. Mineral. 13 (2001) 985–993.
[25] H. Morikawa, I. Minato, T. Tomita, S. Iwai, Anhydrite: a refinement, Acta Crystallogr. Sect. B: Struct. Crystallogr. Cryst. Chem. 31 (1975) 2164–2165, http://dx.doi.org/10.1107/S0567740875007145.
[26] L. Palacios, Á.G. De La Torre, S. Bruque, J.L. García-Muñoz, S. García-Granda, D. Sheptyakov, et al., Crystal structures and in-situ formation study of mayenite electrides, Inorg. Chem. 46 (2007) 4167–4176, http://dx.doi.org/10.1021/IC0700497.
[27] E. Irran, E. Tillmanns, G. Hentschel, Ternesite, $Ca_5(SiO_4)2SO_4$, a new mineral from the Ettringer Bellerberg/Eifel, Germany, locality: Ettringer Bellerberg volcano, Eifel, Germany, Mineral. Petrol. 60 (1997) 121–132.
[28] D.P. Bentz, Activation energies of high-volume fly ash ternary blends: hydration and setting, Cem. Concr. Compos. 53 (2014) 214–223, http://dx.doi.org/10.1016/j.cemconcomp.2014.06.018.
[29] D.P. Bentz, T. Barrett, I. De la Varga, W.J. Weiss, Relating compressive strength to heat release in mortars, Adv. Civ. Eng. Mater. 1 (2012) 1–16, http://dx.doi.org/10.1520/ACEM20120002.
[30] F. Zunino, M. Lopez, A generalized methodology for assessing the chemical and physical potential of industrially sourced rice husk ash on strength development and early-age hydration of cement paste, Cem. Concr. Res. (2016) (Under Review).
[31] D.P. Bentz, P.E. Stutzman, F. Zunino, Low-temperature curing strength enhancement in cement-based materials containing limestone powder, Mater. Struct. (2016) (Under review).
[32] H.F.W. Taylor, Modification of the Bogue calculation, Adv. Cem. Res. 2 (1989) 73–77, http://dx.doi.org/10.1680/adcr.1989.2.6.73.
[33] D.X. Xuan, Z.H. Shui, Rehydration activity of hydrated cement paste exposed to high temperature, Fire Mater. (2010), http://dx.doi.org/10.1002/fam.1067.
[34] J. Barbier, B.G. Hyde, The structures of the polymorphs of dicalcium silicate, Ca_2SiO_4, Acta Cryst B41 (1985) 383–390.
[35] T. Link, F. Bellmann, H.M. Ludwig, M. Ben Haha, Reactivity and phase composition of $CaSiO_4$ binders made by annealing of alpha-dicalcium silicate hydrate, Cem. Concr. Res. 67 (2015) 131–137.
[36] I. Nettleship, J.L. Shull, W.M. Kriven, Chemical preparation and phase stability of Ca_2SiO_4 and Sr_2SiO_4 powders, J. Eur. Ceram. Soc. 11 (1993) 291–298, http://dx.doi.org/10.1016/0955-2219(93)90028-P.
[37] S. Hong, J.F. Young, Hydration kinetics and phase stability of dicalcium silicate synthesized by the Pechini process, J. Am. Ceram. Soc. 82 (1999) 1681–1686, http://dx.doi.org/10.1111/j.1151-2916.1999.tb01986.x.
[38] H. Jennings, J. Thomas, 3.9 synthetic minerals used for research purposes, The Science of Concrete Monograph [Online], Northwestern University Infrastructure Technology Institute, 2008.